

Mapping internal temperatures during high-rate battery applications

T. M. M. Heenan^{1,2}, I. Mombrini^{1,3}, A. Llewellyn¹, S. Checchia³, C. Tan^{1,2}, M. Johnson¹, A. Jnawali¹, G. Garbarino³, R. Jarvis^{1,2}, D. J.L. Brett^{1,2}, M. Di Michiel³, P. R. Shearing^{1,2,Ψ}

Electric vehicles (EV) demand high charge/discharge rates creating potentially dangerous temperature rises. Lithium-ion cells are sealed during their manufacture, making internal temperatures challenging to probe¹. Tracking current collector expansion using X-ray diffraction (XRD) permits non-destructive internal temperature measurements²; however, cylindrical cells are known to experience complex internal strain^{3,4}. Here, we characterise the state-of-charge (SoC), mechanical strain, and temperature within Lithium-ion 18650 cells operated at high rates (>3C) via two advanced synchrotron XRD methods: firstly, as entire cross-sectional temperature maps during open-circuit cooling and secondly, single-point temperatures during charge/discharge cycling. We observed that a 20-minute discharge on an energy-optimised cell (3.5Ah) resulted in internal temperatures >70°C, whereas, a faster 12-minute discharge on a power-optimised cell (1.5Ah) resulted in substantially lower temperatures (< 50°C). However, when comparing the two cells under the same electrical current, the peak temperatures were similar, e.g., a 6A discharge resulted in 40°C peak temperatures for both cell types. We observe that the *operando* temperature rise is due to heat accumulation, strongly influenced by the charging protocol e.g., constant-current (CC) and/or constant-voltage (CV); mechanisms that worsen with cycling, as degradation increases the cell resistance. Design mitigations for temperature-related battery issues should now be explored using this novel methodology to provide opportunities for improved thermal management during high-rate EV applications.

Introduction

The electrification of transport will depend heavily on the improvement of lithium-ion (Li-ion) battery technologies. For example, aviation demands very high discharge rates during flight take-off⁵, and similarly, extreme fast charging of automotive vehicles will be required to mitigate charging-point congestion and downtime for goods transport⁶. To meet these demands many high-rate solutions are emerging⁷⁻⁹, however, thermally induced degradation remains problematic^{10,11}. To advance cell designs such that these degradation issues can be mitigated, we must be able to accurately quantify internal temperatures during operation. This is challenging because cells are sealed during their manufacture for protection from contamination¹² and short-circuit¹³. To non-destructively measure temperature, the thermal expansion of metals¹⁴ such as the current collector² have been measured via X-ray diffraction (XRD), but to resolve internal temperatures directly has required modification of the cell to incorporate thermocouples¹.

Computed tomography (CT) methods allow non-destructive measurements to be resolved spatially¹⁵ and has uncovered many complex distributions of strain³ and SoC⁴. Recently XRD-CT has revealed unprecedented insights into the internal SoC distributions within Li-ion cells¹⁶. Alas, lattice changes due to thermal expansion are orders of magnitude lower than those associated with lithiation. For instance, a 10 °C temperature change in copper would result in a 6×10^{-4} Å lattice parameter expansion, whereas the lattice changes during lithium intercalation (or de-intercalation) of the cathode active material are two to three orders of magnitude greater². Therefore, SoC can be extracted without characterising the thermal and mechanical strain due to their negligible contributions, but resolving temperature requires mechanical and thermal strain deconvolution, and the greater the number of spatial dimensions that are resolved (e.g., 1, 2, 3D) the more complex this becomes.

¹ Electrochemical Innovation Lab, Department of Chemical Engineering, UCL, London WC1E 7JE, U.K.

² The Faraday Institution, Quad One, Harwell Science and Innovation Campus, Didcot, OX11 0RA, U.K.

³ The European Synchrotron, 71 Avenue des Martyrs, 38000, Grenoble, France.

^Ψ Corresponding author: Professor Paul R Shearing, p.shearing@ucl.ac.uk

49 Materials demand is set to expand rapidly with the electrification of transport¹⁷ and two
50 contrasting cathode chemistries are lithium iron phosphate (i.e., LFP or $\text{Li}_{1-x}\text{FePO}_4$) and the layered
51 nickel-rich transition metal oxides (e.g., NMC811 or $\text{Li}_{1-x-y}\text{Ni}_{0.8}\text{Mn}_{0.1}\text{Co}_{0.1}\text{O}_2$). LFP boasts longer
52 lifetimes and enhanced safety, ideal for power-optimised cells; whereas NMC offers higher volumetric
53 and gravimetric energy densities, more suitable for energy-optimised cell designs¹⁸. Similarly, many
54 commercial anodes are fabricated from either graphite (e.g., Gr or Li_xC_6 , Li_xC_{12} , Li_xC_{18}), silicon (e.g.,
55 Si or Li_xSi_y), silicon-oxide (e.g., SiO or $\text{Li}_x\text{Si}_y\text{O}_z$), or a composite of the two (e.g., Gr-Si, Gr-SiO_z). Note
56 that the oxygen content in Si electrodes is often not known, hence it is commonplace to denote the
57 material SiO_z, where z may be zero or negligible¹⁹. Si offers very high theoretical specific capacities
58 however Gr undergoes significantly less expansion during cycling, accompanied by reduced stress²⁰.
59 Therefore, a plethora of materials combinations will compose the global Li-ion battery market, but a
60 comparison of these key materials, which represent examples of power- and energy-optimised cells,
61 can produce a suitable overview.

62 Here, we explain two methods of non-destructive temperature measurements for commercial
63 cylindrical cells (e.g., 18650 format) via monitoring of the expansion/contraction of the Cu current
64 collector crystal structures from XRD. Firstly, full cross-sectional temperature maps can be generated
65 from conducting XRD-CT, ideal for exploring spatial distributions at the end of charge or discharge
66 (e.g., 2D maps). And secondly, a multi-channel-collimator (MCC) can be used to resolve the
67 temperature within arbitrarily selected internal locations (e.g., 1D lines) for real-time quantifications
68 during operation. This article focuses on two contrasting commercially available 18650 cells, one with
69 a Ni-rich NMC811 cathode vs. Gr-SiO_i anode, and a second with an LFP cathode vs. a Gr anode. The
70 subsequent sections will discuss validation of temperature quantifications without electrochemical
71 operation (*ex situ*), then acquisition via XRD-CT (*in situ*), and MCC-XRD (*operando*).
72

73 Ex situ temperatures

74
75 Cylindrical 18650 cells are assembled as jellyrolls as seen in the laboratory X-ray attenuation CT cross-
76 sectional image in **Fig. 1a,b**. A similar cross section can be produced (at a lower spatial resolution) by
77 monitoring the metallic current collector lattice spacing² to calculate the temperature (**Fig. 1c**) and
78 reconstructing a spatially resolved image using XRD-CT (**Fig. 1d,e**). XRD-CT can accurately
79 reconstruct only quantities which are invariant for rotation around the tomographic rotation axis,
80 temperature maps can be obtained since the thermal induced strain is in most materials a scalar quantity.
81 The result is a spatiotemporal map of the internal cell temperature. As a simple proof-of-concept
82 experiment the authors first mapped the internal temperatures within two 18650 cells after heating
83 within a furnace (without electrochemical operation). The internal temperatures are displayed within
84 **Fig. 1** as cross-sectional slices taken from the same region-of-interest (RoI) within the cell as the cells
85 cooled over the course of ca. 30 minutes.

86 The temperature quantifications calculated by fitting the data of the Cu d-spacing closely
87 followed fittings based on Newton's law of cooling (**Fig. 1c**, and see methods), indicating a high level
88 of confidence in the quantifications. To the authors' knowledge, this is the first report of a spatially
89 resolved temperature map within a commercial 18650 Li-ion cell without disassembly or modification.
90 We will now consider the far more complex determination of temperatures driven by electrochemical
91 operation. Note that all error bars throughout this article indicate statistical errors (standard deviation),
92 the precision error is ca. ± 3 °C throughout.

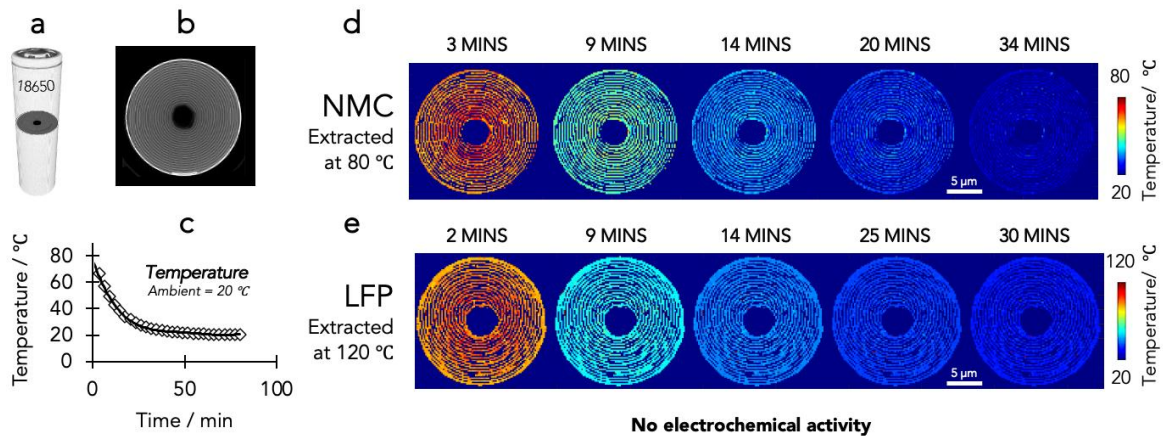


Fig 1. Spatiotemporal temperature mapping within 18650s without electrochemical operation. **a,b,** Laboratory X-ray CT (a) volume render and (b) ortho-slice of the NMC cell displaying the steel casing and internal jellyroll assembly. **c,** Internal temperatures within the NMC cell during cooling immediately after removal from the oven at 80 °C. **d,e,** A similar ortho-slice as shown in the laboratory CT (a) but instead representing the internal cell temperature obtained from synchrotron XRD-CT for (d) the NMC cell removed at 80 °C and (e) the LFP cell removed at 120 °C. Note that ambient temperature was assumed to be a consistent 20 °C.

In situ temperatures

To conduct electrochemical operation while also obtaining temperature measurements via XRD methods, a bespoke 18650 cell holder was designed and optimised to deliver sufficient XRD signal-to-noise (SNR) while also permitting high electrical currents with low circuit losses (**Extended Data Fig. 1**). Examples of the integrated XRD patterns and refinement can be found within the supplementary material (**Extended Data Fig. 2**). Employing this set-up allowed both Coulomb counting of the electrochemical data and XRD analysis of the active electrode materials² to give indications of the SoC, and further, reconstruction via XRD-CT generated spatial maps of the SoC for each material¹⁶. In addition to SoC, mechanical strain information has proven highly important within 18650 cells^{3,4}, and similar to SoC, XRD methods can also be used to extract this mechanical strain. Temperature measurements are the focus of this article but *operando* SoC and mechanical strain calculations can be found within the supplementary material (**Extended Data Fig. 3-7**).

As demonstrated for the oven-heating experiment (**Fig. 1**), internal temperatures could be mapped as 2D cross-sections as the cell cooled. **Fig. 2** displays the temperature values recorded during the transition to open circuit voltage (OCV) after discharge at various rates (approx. temperature peak values shown in **Fig. 2a**). To inspect peak internal thermal gradients the cell was divided into 8 radial zones (rings in **Fig. 2b**) but also compared to 8 azimuthal zones (segments in **Fig. 2c**). Increasing the C-rate from 1C to 3C increased the cell temperature by an additional ~ 40 °C, which overshadowed the influence of any thermal gradients across the 8 radial (and azimuthal) zones, which were on the order of ± 5 °C; this was also true for the LFP cell (**Extended Data Fig. 8**).

Although internal spatial variations are not significant relative to a change in C-rate, these heterogeneities should not be overlooked. For instance, a small up-tick in temperature was observed towards the cell core i.e., furthest from the cell walls. This may prove important when optimising active thermal management techniques or when incorporating/informing high-precision multi-scale modelling, and therefore the authors wish to emphasise that, although spatial variations are small (relative to the influence of C-rate) they should still be considered for accurate prediction and characterisation in future studies.

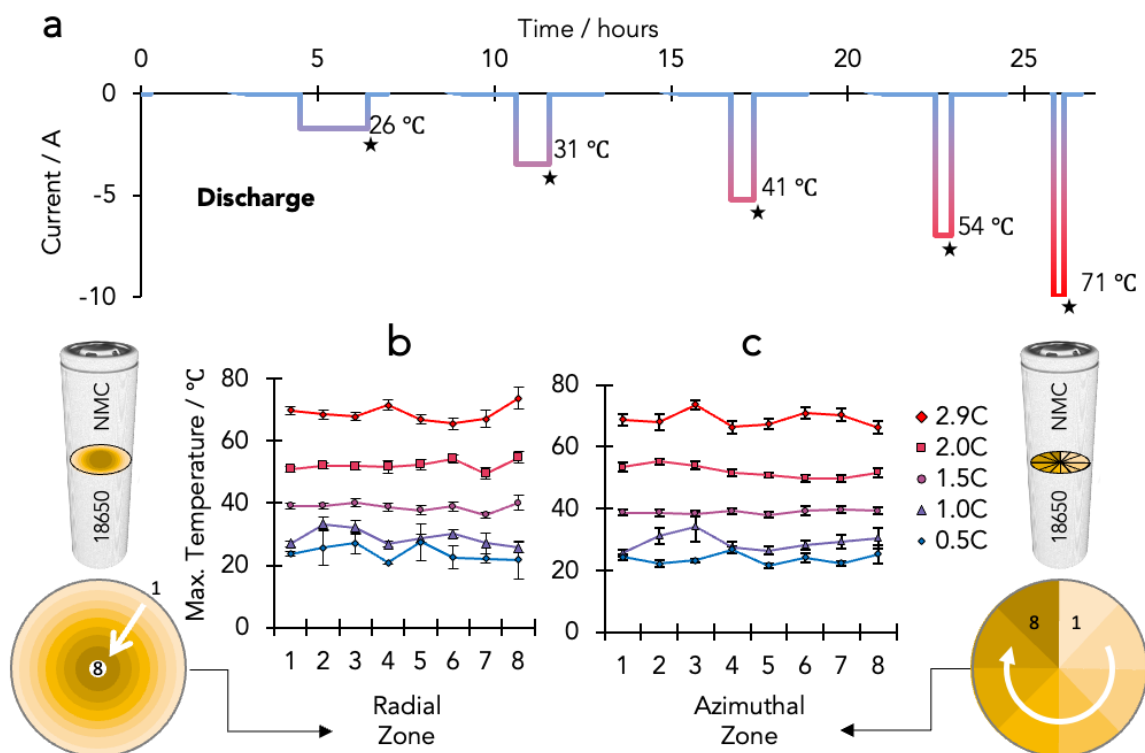
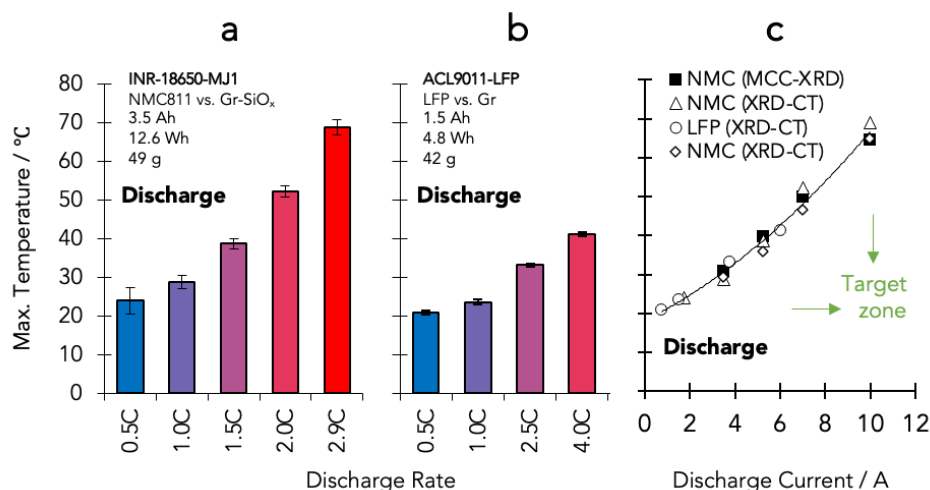


Fig. 2 *In situ* internal temperature maps via XRD-CT. **a**, The high-rate discharge currents for a commercial 18650 with measurement of the peak temperature during the open circuit transition (stars). **b,c**, Internal temperatures for 8 zones divided as (b) radial and (c) azimuthal zones. All error bars are statistical, precision error is ca. ± 3 °C throughout. Note that ambient temperature was assumed to be a consistent 20 °C.

Since the cell capacity dictates the electrical current for a particular C-rate, the contrasting power-optimised 18650 cell (LFP vs. Gr) was also assessed and compared to the energy-optimised counterpart (**Fig. 3a,b**), with the maximum temperature plotted with respect to the discharge current within **Fig. 3c** (circles) alongside two NMC cells (diamonds and triangles). The maximum temperature recorded grew similarly with discharge current irrespective of the cell type, e.g., at a discharge current of 6 A the maximum temperature was approximately 40 °C for all cells regardless of chemistry and this correlation held well throughout all discharge currents explored (i.e., up to approx. 10 A).

The thermal conductivities of the current collectors (assumed to be 398 and 235 W/m/K for copper and aluminium, respectively) are three orders of magnitude higher than the electrodes, and four orders higher than the separator. Therefore, it is unlikely that large amounts of heat are transferred rather through the electrodes or directly through the separator material. Instead, it is more probably that heat is preferentially and efficiently transferred around the jelly-roll winding through the metallic current collectors. Additionally, heat transfer from the interior to the exterior of the cell is very inefficient due to the much lower thermal conductivity of the steel case (~ 45 W/m/K). These factors explain the degree of homogeneity observed throughout the cell in **Fig. 2**, the current collector promotes temperature uniformity via high thermal conduction. Similarly, the strong dependence of the electrical current upon the peak temperature (**Fig. 3**) can be explained by the inefficient thermal properties of the casing design, which promotes heat accumulation, and the subsequent temperature rises. See further discussions within the Supplementary Material. This also indicates that Joule heating (at least for high currents) dominates heat generation, rather than reaction heating. Power-optimised LFP chemistries, with lower capacities, therefore present a favourable heat (and temperature) management option for high-rate applications since a lower relative electrical current can achieve a higher C-rate, thus faster charge/discharge and SoC change, although at the cost of lower energy densities. Therefore, if onboard energy density can be compromised, i.e., if shorter driving or flight ranges are acceptable in certain applications e.g., agricultural drones or warehouse robots, power-optimised cells such as these can offer improved thermal management.

164 The similarities of peak temperatures within the two cells at various discharge currents suggests
 165 that fundamental cell design alterations would be required to mitigate high temperatures (via improved
 166 heat dissipation) during high electrical currents, i.e., to enter the green ‘target zone’ visualised in **Fig**
 167 **3c**. Consequently, the authors concluded that a method for understanding *operando* temperature
 168 changes (i.e., measurements during charge transfer) would be essential to explore how the heat is
 169 accumulated during operation.



170 **Fig. 3** *In situ* internal temperature maxima via XRD-CT. **a,b**, The internal temperature maxima
 171 within the commercial (a) energy- and (b) power-optimised cells immediately after discharge at various C-rates.
 172 **c**, The maximum internal temperature correlated with discharge current for two energy cells and one power cell,
 173 obtained at the end of discharge/start of OCV, via XRD-CT or MMC-XRD. Note that ambient temperature was
 174 assumed to be a consistent 20 °C.

177 *Operando* temperatures

178 During cell charge and discharge, in addition to thermal strain due to the Joule heating effect, the Cu
 179 current collector develops mechanical elastic strain caused by stress build up inside the cell, originated
 180 by different volumetric expansion/contraction of anode and cathode. To separate the mechanical from
 181 thermal strain and explore the temperature during stages that precede the peak temperatures reported in
 182 **Fig 3**, the methodology for a second XRD measurement was developed by employing a Multi-Channel
 183 Collimator (MCC) (**Extended Data Fig. 9**) which allows high speed (sub-second), high angular
 184 resolution and high SNR XRD measurements from a given spatial location (gauge volume). MCC-XRD
 185 measurements were performed along the same radial line, at two orthogonal orientations of the cell.

186 The *operando* MCC current collector tangential and radial strain measurements, combined with
 187 *operando* XRD-CT axial strain measurements permitted the analysis of temperature dynamics during
 188 the whole charge/discharge process, not only during open circuit. **Fig. 4** displays the temperature values
 189 recorded for zone 4 within an NMC cell during four charge-discharge cycles, whereby all four charges
 190 were conducted at 1C but each discharge was increased until the manufacturer’s specified maximum
 191 electrical current of c. 10 A was reached. For completeness, **Fig. 3c** also reports the MCC data, showing
 192 close agreement with the XRD-CT values. The temperature and radial stress during the four charge
 193 profiles (at 1C, 3.5 A) were highly repeatable with minimal variation (**Fig. 4a,b**). Furthermore, the
 194 transition (dashed vertical line, ca. 45 mins) between the constant current (CC) and constant voltage
 195 (CV) stages was clearly distinguishable.

196 During CC the temperature rises due to the heat accumulation but once the current is allowed
 197 to decay under CV (or OCV) the temperature reduces, as heat loss to the surroundings exceeds that
 198 generated due to Joule heating. Consequently, there is a clear correlation between the electrical current
 199 employed and the temperature rise observed (as shown in **Fig. 4a**) but subsequently, the internal
 200 temperature at the end of charge will be dictated by the profile of the electrical current over the entire
 201 duration of the charge profile. For instance, other charging protocols such as current pulse or constant
 202

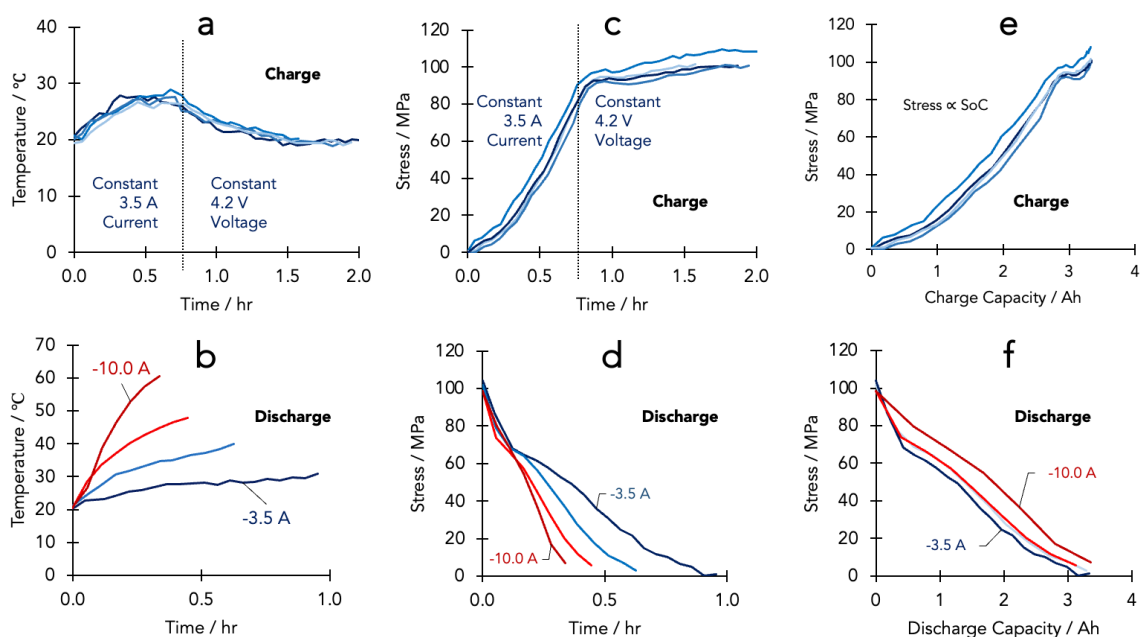
203 power may produce different temperature profiles to that seen here (under CC-CV) because the trade-
204 off between heat generation and loss (to the surroundings) is different.

205 Discharge was conducted without a CV hold, i.e., only under CC. The temperature rise during
206 the CC discharge followed a similar (but inverted) profile to the cooling after removal from the oven in
207 the first experiment (compare heating in **Fig. 4b** to cooling in **Fig. 1d**); whereby initially the temperature
208 changes rapidly but then slowing with time.

209 Naturally, unlike the thermal dynamics, the mechanical stress does not reduce during the CV
210 stage due to the intercalation (and de- intercalation) mechanisms occurring during charge (**Fig. 4c**). This
211 stress is only relieved once the discharge process is completed (**Fig. 4d**). Marginal stress hysteresis,
212 observed as non-zero stress values at the end of discharge, may be attributed to the inaccessible
213 discharge capacities at higher rates (**Extended Data Fig. 7**). It should also be noted that stress was most
214 dependent upon the SoC (see stress-capacity in **Fig. 4e,f**) and showed no correlation with C-rate (**Fig.**
215 **4f**).

216 It should also be noted that it is possible (through the collection of temporally resolved
217 temperature data) to calculate effective heat transfer coefficients. By exploring the temperature decay
218 time (τ), assuming the cell mass to be 49 g, and the cell to be sufficiently represented by a perfect
219 cylinder i.e., flat caps, using a reference for the cell heat capacity e.g., 960 J / kg / K from Maleki *et*
220 *al.*²¹, the heat transfer coefficient for the energy cell is calculated to be ca. 17.6 W / m² / K. Full workings
221 can be found within the Methods. Such calculations may inform cell and pack computational modelling
222 in predictive studies, that in turn, may inform future experiments.

223



224

225

226 **Fig. 4** *Operando* internal temperatures via MCC-XRD. **a,b**, The temperature during (a) charge and
227 (b) discharge for the four cycles. **c,d**, The stress during (c) charge and (d) discharge for the four cycles. **e,f**,
228 Assessing the relationship between the SoC (capacity) and the stress for the four (e) charge cycles all at 1C and
229 (f) discharge cycles at various C-rates. Note that ambient temperature was assumed to be a consistent 20 °C.

230

231 Temperatures after degradation

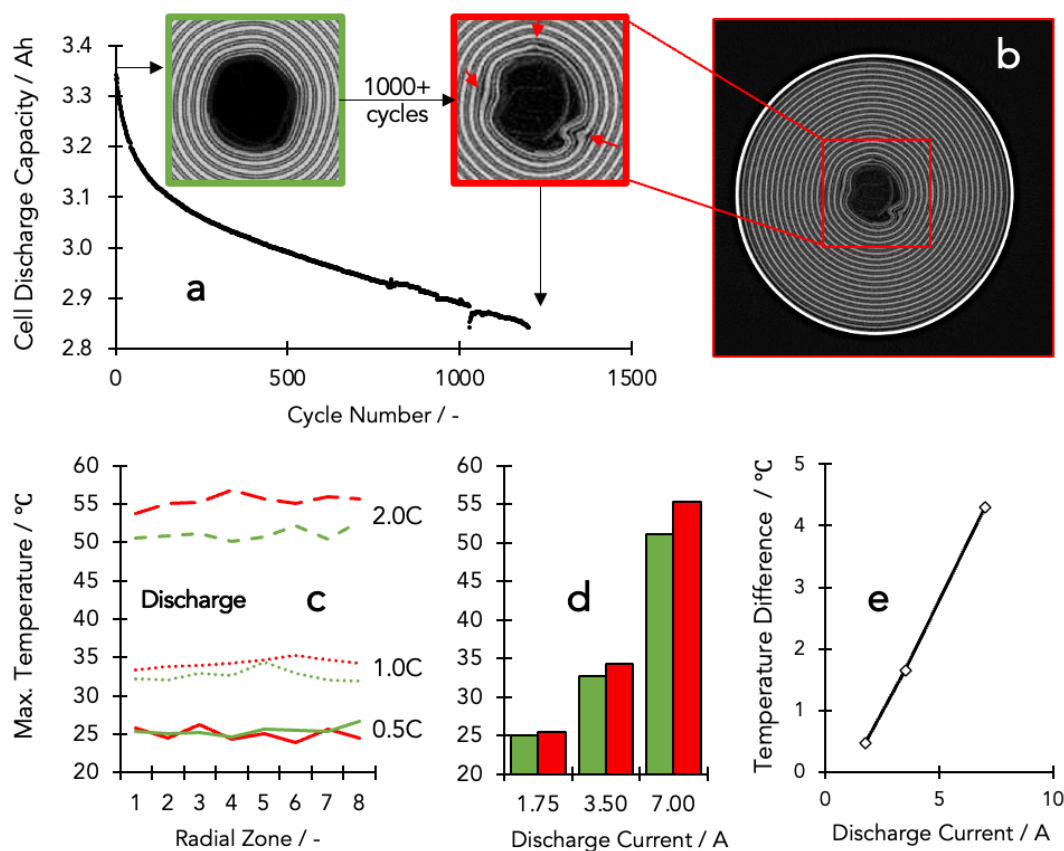
232

233 The characterisation of cell temperatures is important not only at the beginning of use but throughout
234 the cell's lifetime. So, in addition to exploring temperatures extracted from pristine cells i.e. as supplied
235 from the manufacturer; **Fig. 5** presents insight into the implications for thermal management after
236 significant operation (e.g. beyond 1,000 operational cycles).

237 Firstly, prolonged cycling is known to lead to increased resistance as a result of cell degradation
 238 that restricts the accessible cell capacity¹⁸ (see the discharge capacity loss with each operational cycle,
 239 **Fig. 5a**). To translate this to real-world applications, this means that the total driving range for an EV
 240 will decrease with each recharge (assuming controlled conditions e.g., no substantial temperature
 241 changes, etc.). Many degradation mechanisms can be observed in the form of microstructural changes
 242 as seen in the magnified cell contents in **Fig. 5a**, and the full cross-section in **Fig. 5b**.

243 **Fig. 4b** provides an indication of the possible implications of degradation on cell temperatures.
 244 The longer the cell is held at constant current, the higher the internal temperature rise, i.e. the internal
 245 cell temperature correlates with the magnitude of the current and the time spent at CC (units ampere-
 246 hour, Ah). This gives rise to two key probabilities for degraded cells based upon their discharge
 247 capacity. Scenario 1: capacity remains high (e.g. >80%), thus can still withstand a significant time at
 248 CC but under a higher internal resistance, producing more heat and higher temperatures than pristine.
 249 Scenario 2: capacity has declined significantly (e.g. <80%), thus cannot withstand significant time at
 250 CC, thus even with substantial internal resistance, produces lower temperatures than pristine. The real-
 251 world consequence of scenario 2 is possibly a warranty failure of the EV, the battery would require
 252 replacement; whereas the significantly more serious consequence of scenario 1 is the potential
 253 compromise of the safety measures designed for pristine cells, endangering the user.

254 **Fig. 5c** provides an example of scenario 1. The visibly degraded cell (**Fig. 5a,b**) exhibits signs
 255 of delamination and cracking at the cell-level which gives rise to a higher internal temperature after
 256 discharge that is most notable at higher C-rates (**Fig. 5c**) and electrical currents (**Fig. 5d**). Under a 7 A
 257 discharge the aged sample was ca. 4 °C higher than the pristine, a consistent but small increase relative
 258 to the influence of C-rate e.g. doubling the C-rate from 1 to 2C resulted in an additional temperature
 259 rise of approx. 30 °C. Nonetheless, a plethora of degradation mechanisms are known to elevate cell
 260 internal resistances, and this is only one example. Future studies may explore other chemistries,
 261 geometries, microstructures and charging protocols.



262 **Fig. 5** *Internal temperatures after cycling.* **a,b**, The (a) electrochemical and (b) structural data from
 263 an energy-optimised 18650 3.5 Ah nominal capacity cell before (green) and after (red) long-duration cycling. **c**,
 264 The maximum temperature recorded for the eight radial zones. **d**, The average temperature immediately after each
 265

266 discharge current. e, The difference between the cycled and pristine cell temperatures after three discharge
267 currents. Note that ambient temperature was assumed to be a consistent 20 °C.
268

269 **Future thermal management**

270
271 In conclusion, 1D point and 2D mapping measurements² have provided substantial insight into the
272 possibilities of thermo-mechanical characterisations of operational cells, however, are inherently
273 restricted in the information that can be extracted. The ability to resolve additional spatial dimensions
274 (3D), permitting internal measurements and the decoupling of thermal from mechanical contributions
275 to electrochemical changes, as presented here, offers a step-change advancement in the possible insight
276 available. For instance, internal distributions (see Fig.1,2) are only possible with spatially resolved
277 methods (i.e., 3D). Moreover, incorporating bespoke set-ups (e.g., MCC) allow suitable measurement
278 precision whilst under fast operation dynamics (i.e., internal *operando* studies).

279 We present here two methodologies to accurately (± 3 °C) quantify internal temperatures during
280 high-rate (up to 10.0 A) operation of commercial Li-ion 18650s without cell modification or
281 disassembly. These methods should be applicable to the vast majority of, if not all, commercial 18650s,
282 and may be conducted by any specialist XRD synchrotron beamline with the cell holder (described
283 within the methodology and supplementary) and using the correct imaging setup. Moreover, minor
284 alterations would permit the study of other cell geometries, e.g., 2170 and 4680, and non-standard
285 microstructures e.g., ultra-thin current collectors.

286 Temperature mapping using XRD-CT revealed that the peak temperatures reached within the
287 cell are relatively homogeneous (spatially) at the end of discharge and the magnitude of this temperature
288 peak is largely dictated by the electrical current employed. The MCC-XRD temperature mapping
289 method then revealed that this temperature peak is reached due to an accumulation of heat and is
290 strongly influenced by the charging protocol (e.g., the use of CC or CC-CV, etc.). Finally, we discuss
291 the implications for used cells (e.g. 1,000+ cycles), proposing two key undesired scenarios. The first
292 where cells can no longer withstand high currents, thus are unable to generate large amounts of Joule
293 heating, and are therefore likely to fail warranty and require replacement. The second scenario has
294 potential safety implications, where cells that are still able to receive high electrical currents but also
295 experience significantly higher internal resistance than in their pristine state, produce increased heat
296 and higher internal temperatures potentially endangering the user. Future studies may expand upon
297 these scenarios with real-time quantifications that can inform computational modelling^{22,23}, potentially
298 with the inclusion of statistical analysis indicating the probability of each scenario.
299

300 **References**

- 301
302 1. Spinner, N., et al. Novel 18650 lithium-ion battery surrogate cell design with anisotropic
303 thermophysical properties for studying failure events. *Journal of Power Sources*. Volume 312,
304 Pages 1-11 (2016).
305 <https://doi.org/10.1016/j.jpowsour.2016.01.107>
306
307 2. Yu, X., et al. Simultaneous Operando Measurements of the Local Temperature, State of
308 Charge, and Strain inside a Commercial Lithium-Ion Battery Pouch Cell. *J. Electrochem. Soc.*
309 165 A1578 (2018).
310 <https://doi.org/10.1149/2.1251807jes>
311
312 3. Kok, M., et al. Virtual unrolling of spirally-wound lithium-ion cells for correlative
313 degradation studies and predictive fault detection. *Sustainable Energy Fuels*, 3, 2972-2976
314 (2019).
315 <https://doi.org/10.1039/C9SE00500E>
316
317 4. Ziesche, R.F., Arlt, T., Finegan, D.P. et al. 4D imaging of lithium-batteries using correlative
318 neutron and X-ray tomography with a virtual unrolling technique. *Nat Commun* 11, 777
319 (2020).

- 320 <https://doi.org/10.1038/s41467-019-13943-3>
321
322 5. Sripad, S., Bills, A. & Viswanathan, V. A review of safety considerations for batteries in
323 aircraft with electric propulsion. *MRS Bulletin* 46, 435–442 (2021).
324 <https://doi.org/10.1557/s43577-021-00097-1>
325
326 6. Li, M., et al. Fast Charging Lithium-ion Batteries for a New Era of Electric Vehicles. *Cell*
327 *Reports Physical Science*. Volume 1, Issue 10, 100212 (2020).
328 <https://doi.org/10.1016/j.xcrp.2020.100212>
329
330 7. Tomaszewska, A., et al. Lithium-ion battery fast charging: A review. *eTransportation*.
331 Volume 1, 100011 (2019).
332 <https://doi.org/10.1016/j.etrans.2019.100011>
333
334 8. Griffith, K.J., et al. Niobium tungsten oxides for high-rate lithium-ion energy storage. *Nature*
335 559, 556–563 (2018).
336 <https://doi.org/10.1038/s41586-018-0347-0>
337
338 9. Billaud, J., et al. Magnetically aligned graphite electrodes for high-rate performance Lithium-
339 ion batteries. *Nat Energy* 1, 16097 (2016).
340 <https://doi.org/10.1038/nenergy.2016.97>
341
342 10. Lain, M. & Kendrick, E. Understanding the limitations of lithium ion batteries at high rates.
343 *Journal of Power Sources*. Volume 493, 229690 (2021).
344 <https://doi.org/10.1016/j.jpowsour.2021.229690>
345
346 11. Ma, S., et al. Temperature effect and thermal impact in lithium-ion batteries: A review. *Progress*
347 *in Natural Science: Materials International*. Volume 28, Issue 6, Pages 653-666 (2018).
348 <https://doi.org/10.1016/j.pnsc.2018.11.002>
349
350 12. Finegan, D., et al. Tracking Internal Temperature and Structural Dynamics during Nail
351 Penetration of Lithium-Ion Cells. *J. Electrochem. Soc.* 164 A3285 (2017).
352 <https://doi.org/10.1149/2.1501713jes>
353
354
355 13. Han, A., et al. Effect of Humidity on Properties of Lithium-ion Batteries. *Int. J. Electrochem.*
356 *Sci.*, 16, Article ID: 210554, (2021).
357 <https://doi.org/10.20964/2021.05.54>
358
359 14. Hagart-Alexander, C. *Instrumentation Reference Book (Fourth Edition)*, Chapter 21 -
360 Temperature Measurement. Pages 269-326 (2010).
361 <https://doi.org/10.1016/B978-0-7506-8308-1.00021-8>
362
363 15. Houx, J. L., Kramer, D. X-ray tomography for lithium ion battery electrode characterisation
364 — A review. *Energy Reports*, Volume 7, Supplement 2, Pages 9-14 (2021).
365 <https://doi.org/10.1016/j.egyrs.2021.02.063>
366
367 16. Petz, D., et al. Lithium distribution and transfer in high-power 18650-type Lithium-ion cells at
368 multiple length scales. *Energy Storage Materials*. Volume 41, Pages 546-553 (2021).
369 <https://doi.org/10.1016/j.ensm.2021.06.028>
370
371 17. Xu, C., et al. Future material demand for automotive lithium-based batteries. *Commun Mater*
372 1, 99 (2020).
373 <https://doi.org/10.1038/s43246-020-00095-x>
374

- 375 18. Ding, Y., et al. Automotive Lithium-ion Batteries: Current Status and Future Perspectives.
376 Electrochem. Energ. Rev. 2, 1–28 (2019).
377 <https://doi.org/10.1007/s41918-018-0022-z>
378
- 379 19. Heenan, T., et al. Identifying the Origins of Microstructural Defects Such as Cracking within
380 Ni-Rich NMC811 Cathode Particles for Lithium-Ion Batteries. Advanced Energy Materials.
381 Volume 10, Issue 47, 2002655 (2020).
382 <https://doi.org/10.1002/aenm.202002655>
383
- 384 20. Finegan, D., et al. Spatially Resolving Lithiation in Silicon–Graphite Composite Electrodes
385 via in Situ High-Energy X-ray Diffraction Computed Tomography. Nano Lett., 19, 6, 3811–
386 3820 (2019).
387 <https://doi.org/10.1021/acs.nanolett.9b00955>
388
- 389 21. Maleki, H., et al., thermal Properties of Lithium-Ion Battery Components. J. Electrochem.
390 Soc. 146 947 (1999).
391 <https://doi.org/10.1149/1.1391704>
392
- 393 22. Tranter, T., et al. Communication—Prediction of Thermal Issues for Larger Format 4680
394 Cylindrical Cells and Their Mitigation with Enhanced Current Collection. J. Electrochem.
395 Soc. 167 160544 (2020).
396 <https://doi.org/10.1149/1945-7111/abd44f>
397
- 398 23. Offer, G., et al. Cool metric for lithium-ion batteries could spur progress. Nature 582, 485-
399 487 (2020).
400 <https://doi.org/10.1038/d41586-020-01813-8>

401 **Figure legends**

402

403 **Fig 1. Spatiotemporal temperature mapping within 18650s without electrochemical operation.**

404 **a,b**, Laboratory X-ray CT (a) volume render and (b) ortho-slice of the NMC cell displaying the steel casing and

405 internal jellyroll assembly. **c**, Internal temperatures within the NMC cell during cooling immediately after removal

406 from the oven at 80 °C. **d,e**, A similar ortho-slice as shown in the laboratory CT (a) but instead representing the

407 internal cell temperature obtained from synchrotron XRD-CT for (d) the NMC cell removed at 80 °C and (e) the

408 LFP cell removed at 120 °C. Note that ambient temperature was assumed to be a consistent 20 °C.

409

410 **Fig. 2 *In situ* internal temperature maps via XRD-CT. a**, The high rate discharge currents for a

411 commercial 18650 with measurement of the peak temperature at the point of open circuit (stars). **b,c**, Internal

412 temperatures for 8 zones divided as (b) radial and (c) azimuthal zones. All error bars are statistical, precision error

413 is ca. ± 3 °C throughout. Note that ambient temperature was assumed to be a consistent 20 °C.

414

415 **Fig. 3 *In situ* internal temperature maxima via XRD-CT. a,b** The internal temperature maxima

416 within the commercial (a) NMC and (b) LFP cells immediately after discharge at various C-rates. **c**, The max

417 internal temperature correlated with discharge current for two NMC cells and the LFP cell, obtained at the start

418 of open-circuit/end of discharge, obtained either via XRD-CT or MMC-XRD. Note that ambient temperature was

419 assumed to be a consistent 20 °C.

420

421 **Fig. 4 *Operando* internal temperatures via MCC-XRD. a,b**, The temperature during (a) charge and

422 (b) discharge for the four cycles. **c,d**, The stress during (c) charge and (d) discharge for the four cycles. **e,f**,

423 Assessing the relationship between the SoC (capacity) and the stress for the four (e) charge cycles all at 1C and

424 (f) discharge cycles at various C-rates. Note that ambient temperature was assumed to be a consistent 20 °C.

425

426

427 **Methods**

428

429 **18650 Li-ion cells.** The commercial cell testing was performed on 3.5 Ah nominal capacity LG Chem
430 INR-18650-MJ1 cells (Nkon, Netherlands). These cells are assembled using nickel-rich
431 ($\text{LiNi}_{0.8}\text{Mn}_{0.1}\text{Co}_{0.1}\text{O}_2$) cathodes and composite graphite-silicon anodes. Where stated, a comparison cell
432 was also analysed: the 1.5 Ah nominal capacity ACL9011, composed of a lithium iron phosphate (LFP)
433 cathode and graphite anode.

434

435 **Laboratory X-ray CT.** The lab X-ray CT data was collected using a Nikon XT H225 (Nikon
436 Metrology, Inc. U.S.A.) by rotating the sample through 2,278 angular projections and exposing the
437 sample at each increment to a polychromatic X-ray beam of characteristic peak energy of 58 keV (W-
438 $K\alpha$), each with an exposure time of 1 s; with an isotropic 36 μm reconstructed voxel length. This data
439 has been published openly elsewhere and is free to download²³. All data was reconstructed using
440 commercial software employing cone-beam filtered-back-projection (FBP) algorithms ("CT Pro 3D,"
441 Nikon Metrology, Inc. U.S.A.).

442

443 **Laboratory data visualisation.** All lab data was visualised using Avizo Fire software (Avizo, Thermo
444 Fisher Scientific, Waltham, Massachusetts, U.S.A.). Volume renders and ortho-slice cross-sections
445 were generated based upon the raw, unprocessed greyscale data within the tomogram.

446

447 **Synchrotron.** All synchrotron experiments were performed at the ID15A beamline²⁴ at the ESRF – The
448 European Synchrotron, Grenoble, France. During the XRD-CT measurements the sample was
449 continuously rotated while being translated horizontally across the X-ray beam path in steps defined by
450 the horizontal beam size (**Extended Data Fig. 1**). The MCC-XRD data was collected during translation
451 of the sample along either the direction parallel to the beam (x) or perpendicular (y). In both setups the
452 scattered signal was collected at rates of 200-250 Hz using a Pilatus 3X CdTe 2M detector (Dectris,
453 Baden-Dättwil, Switzerland).

454

455 **Multi-Channel Collimator (MCC).** The MCC used in this work consists of two concentric sets of slits
456 radially aligned around the centre of rotation of the diffractometer. The two sets of slits consist of
457 tungsten carbide blades supported by a stainless-steel frame. They contain 75 slits, separated by 0.8°,
458 with a distance of 50 and 200 mm respectively from the sample.²⁸ Thanks to this geometry it is possible
459 to select the scattering signal from an internal volume in the sample (**Extended Data Fig. 9**). The gauge
460 volume from which the diffraction signal is measured is given by the intersection of the primary X-ray
461 beam with the volume seen by the detector through the MCC slits (**Extended Data Fig. 9**). The
462 dimension of the gauge volume full-width-half-maximum (FWHM) along x axis (δx) is approximated
463 by the formula as:

464

465 Equation 1
$$\delta x = \frac{a}{\left(1 - \frac{r_1}{r_2}\right) \sin 2\theta} + \frac{\delta y}{\tan 2\theta},$$

466

467 Where, $a = 50 \mu\text{m}$ is the width of the inner slits; r_1 and r_2 are the inner and outer slit radii, respectively;
468 and δy is the horizontal beam size. As shown by equation 1, the gauge volume varies with the diffraction
469 angle, 2θ . The gauge volume dimensions along y and z directions correspond to the X-ray beam cross
470 section. Sample diffraction patterns without and with multichannel collimator are compared in
471 **Extended Data Fig. 10**.^{28,29}

472

473

474 **Commercial 18650 cell holder.** All *in situ* and *operando* measurements were conducted using the same
475 cell set-up during operational charge-discharge cycling (**Extended Data Fig. 1**), allowing
476 crystallographic information to be resolved internally through various stages of operation. This holder
477 was capable of handling up to 20 A of continuous electrical current, which should encompass the
478 majority of commercial 18650 cell C-rate capabilities. Note that these experiments were limited to 10
479 A due to the potentiostat limit. No thermal management method was applied to the cells during these

480 experiments. The cells were allowed to cool via natural convection cooling to the surroundings. There
481 would be however, scope to integrate both external heating and/or cooling systems for future studies.
482 For example, a heating furnace could be employed to emulate pre-heating conditions and fan cooling
483 could emulate ‘active’ thermal management methods, both of which may provide closer simulations to
484 cells within a battery module.

485
486 **Electrochemistry.** The cells were cycled using a Biologic SP300 cycler with 10 A booster (Biologic,
487 France). The first XRD-CT experiments were conducted on an NMC cell discharged at: 0.5C (1.75 A),
488 1.0C (3.50 A), 1.5C (5.25 A), 2.0C (7.00 A), and 2.9C (9.96 A). The first charge was conducted at 0.5C
489 (1.75 A) in order to begin the discharge experiments, all subsequent charges were conducted at 1.0C
490 (3.5 A). After each charge or discharge step, the cell was held at OCV for 30 mins. This was repeated
491 with a second NMC cell. The second XRD-CT experiment was conducted on an LFP cell discharged
492 at: 0.5C (0.75 A), 1.0C (1.50 A), 2.5C (3.75 A), 4.0C (6.00 A), and 5.0C (7.50 A). The first charge was
493 conducted at 0.5C (0.75 A) in order to begin the discharge experiences, all subsequent charges were
494 conducted at 1.0C (1.5 A). After each charge or discharge step, the cell was held at OCV for 30 mins.
495 The MCC-XRD experiment was conducted on an NMC cell discharged at: 1.0C (3.50 A), 1.5C (5.25
496 A), 2.0C (7.00 A), and 2.9C (10.0 A). The first charge was conducted at 0.5C (1.75 A) in order to begin
497 the discharge experiences, all subsequent charges were conducted at 1.0C (3.5 A). After each charge or
498 discharge step, the cell was held at OCV for 30 mins.

499
500 **Ex situ temperatures.** The *ex situ* oven-heating experiments were performed using ultra-fast XRD-CT
501 with an incident beam energy of 95 keV and a 200 x 200 μm^2 beam size. The detector-sample distance
502 was set to 1000 mm. XRD-CT scans were performed every \sim 170 seconds. After keeping the LFP cell
503 at 120 °C for three hours, XRD-CT data was collected over the course of 1.25 hours while the cell was
504 cooling to room temperature with no electrochemistry applied. The same measurements were performed
505 every \sim 255 seconds on an NMC811 cell, during cooling in air, after holding at 80 °C for three hours.

506
507 **In situ temperature measurements.** The *in situ* OCV cooling experiments were performed using ultra-
508 fast XRD-CT while charging and discharging the cell at different rates. The experiments were
509 conducted using an X-ray beam of 100 keV and a 200 x 200 μm^2 size, XRD-CT scans were performed
510 every 3 minutes. The detector-sample distance was set to 1275 mm for NMC cells, and 1770 mm for
511 LFP cells. XRD-CT datasets were collected continuously during charge/discharge for the entire
512 electrochemical cycle on each cell. The cell mounted in the battery holder was connected to the Biologic
513 SP300 potentiostat.

514
515 **Operando temperature measurement.** The *operando* experiments were performed using MCC-XRD.
516 These experiments employed an incident beam energy of 95 keV and a 200 x 25 (VxH) μm^2 beam size
517 to attain a narrow gauge-volume. The cell, mounted in the battery holder, was connected to the Biologic
518 SP300 potentiostat. The detector-sample distance was set to 1000 mm. The sample was translated
519 alternately perpendicular and parallel to the incident beam, collecting multiple diffraction points to
520 select different Cu current collector spirals in each scan.

521
522 **XRD-CT reconstruction.**
523 It should be noted that, data was acquired over 360° rotations in order to obtain the correct centre of
524 mass for the Cu diffraction peaks (i.e. without the artefacts that would be introduced via traditional 180°
525 rotation acquisition on a large sample). To accurately determine the Cu lattice parameter changes and
526 the temperature only Cu peaks not overlapping with peaks from other cell components (NMC811, Al,
527 Steel, etc) were considered. For each measured XRD-CT slice, the 2D diffraction patterns $I(2\theta, \eta)$ from
528 all rotation and translation positions were integrated over the azimuthal angle (η) using pyFAI
529 software²⁵. The azimuthal range was $\pm 15^\circ$ around the vertical scattering plane, corresponding to a
530 condition where the momentum transfer vector (\mathbf{q}) is virtually parallel to the sample rotation axis (z ,
531 see **Extended Data Fig. 1**). The resulting azimuthally integrated data was corrected for incident flux
532 and sample absorption effects and finally reconstructed through a FBP algorithm implemented in
533 Matlab (Mathworks, Cambridge, U.K.). The Cu 111 and 200 diffraction intensities were consistent

534 along the $(-\pi, \pi)$ range of azimuthal angle, without indications of peaking at certain azimuthal angles,
535 consequently it was considered that diffraction texture did not detrimentally impact the tomographic
536 reconstructions.

537
538 **Temperature calculations.** To calculate internal cell temperatures, position of Cu Bragg peaks were
539 calculated for each voxel in the tomograms and for each of the MCC scans. Peak centre of mass
540 calculations gave accurate d -spacings for the available Cu reflections in the different sample/setup
541 combinations used. To inspect internal thermal gradients, spatially resolved data were binned into eight
542 circular regions inside the battery based on their radial position between the internal and the external
543 border of the active area (**Fig. 2b**). Eight azimuthal regions were also defined as shown in **Fig. 2c**. To
544 reduce the statistical error, the mean values were calculated for each region as function of time. The
545 temperature generated from the C-rate discharge applied to the cell in the 8 zones (radial and azimuthal)
546 was calculated by fitting the data of Cu d -spacing from the end of the discharge until the end of the
547 following rest based on Newton's law of cooling. Since the XRD-CT data were taken during OCV in
548 the discharge state, it was assumed that no strains were contributing to the contraction of the Cu crystal
549 lattice during cooling. The function used for the fitting was an exponential decay:

550
551 Equation 2
$$d(t) = d_0 - \Delta d \cdot e^{-\frac{t-t_0}{\tau}}$$

552
553 Where t is the time, t_0 the time at which the discharge finished, τ the decay time, Δd the total d -spacing
554 variation of a given Bragg reflection of the Cu current collector, d_0 is the d -spacing at time t_0 .
555 Temperature variation ΔT inside the battery at the end of each discharge for the eight zones was
556 calculated from the relative change in d -spacing using Equation 3. The thermal expansion coefficient
557 of Cu was experimentally determined through temperature-dependent XRD on a fragment of the current
558 collector extracted from a 18650 cell.

559
560 Equation 3
$$\Delta T = \frac{1}{\alpha} \frac{\Delta d}{d_0}$$

561
562 **Strain calculations.** The positions of Cu Bragg peaks used for internal temperature calculations were
563 also used to calculate strain values. Likewise, the battery section was split into eight radial zones and
564 values from the voxels in each zone averaged for better statistics. Strain on Cu current collector caused
565 by the volume change due to lithiation of graphite was calculated by measuring the Cu d -spacing before
566 the charge (d_0) and the Cu d -spacing after the charge (d). The final strain after charge was calculated
567 for the eight circular zones inside the battery with the following equation:

568
569 Equation 4
$$\varepsilon = \frac{d-d_0}{d_0}$$

570
571
572 **Rietveld refinements.** Rietveld analysis was performed on the $I(2\theta)$ patterns in the reconstructed
573 tomograms of the cells to calculate the SoC from the varying distribution of lithiated anode phases.
574 Batch fit routines were set up in Topas v7²⁶ to handle the analysis of the several thousands of
575 diffractograms in each dataset. While the refinement strategy was unconstrained (i.e., letting structural
576 parameters vary within a suitable range), care must be applied when setting parameter limits and initial
577 values in order to ensure that the fit converges and avoids local minima. The fitted model comprised a
578 2-parameter Chebyshev polynomial background and four rhombohedral graphite-like phases
579 (delithiated graphite and lithiation stages I, II, III). Each phase had refinable lattice parameters, scale
580 factor and one peak-width parameter, whose $\tan(2\theta)$ -dependent broadening was convoluted with a
581 fixed Pseudo-Voigt contribution previously refined on the calibrant powder (NIST SRM 674b Cr_2O_3)
582 to yield the final peak shape.

583
584 **SoC calculations.** The number of moles of Li per mole of C_6 was calculated from the mass fractions of
585 the lithiation stages determined by Rietveld analysis.²⁷ The diffraction patterns were consistent with a
586 choice of four stages: graphite, Stage III, Stage II, and Stage I. Stage III was considered as a solid

587 solution whose Li content varied linearly with the lattice parameter c between LiC_{19} and LiC_{30} . The
 588 stoichiometries of Stage II and Stage I were LiC_{12} and LiC_6 , respectively. The lithiation state x in Li_xC_6
 589 was calculated as:
 590

591 Equation 5
$$x = 6 \times \frac{\frac{\sum_{s=1}^3 m_s f_s}{w_{\text{Li}}}}{\frac{m_g + \sum_{s=1}^3 m_s (1-f_s)}{w_{\text{C}}}}$$

592 Here w_{Li} and w_{C} are the atomic weights of Li and C; m_g the mass fraction of graphite; m_s the mass
 593 fraction of phase s (lithiation stages I-III); f_s the mass fraction of Li in the same phases.
 594

595 The calculation of the effective heat transfer coefficient was as follows:
 596
 597

598 Equation 6
$$T(t) = T_{\text{ambient}} + (T_{\text{max}} - T_{\text{ambient}}) * \exp\left(\frac{-t \times h \times A}{m \times C_p}\right)$$

599
 600 T temperature
 601 t time
 602 h heat transfer coefficient
 603 A cell surface area
 604 m cell mass
 605 C_p cell heat capacity
 606

607 Fits were performed on the experimental data using this formula:
 608

609 Equation 7
$$T(t) = T_{\text{ambient}} + (T_{\text{max}} - T_{\text{ambient}}) * \exp\left(\frac{-t}{\tau}\right)$$

610
 611 τ temperature decay time
 612

613 Solving Equations 6 and 7:
 614

615 Equation 8
$$\frac{1}{\tau} = \frac{h \times A}{m \times C_p}$$

616
 617 Solving for h:
 618

619 Equation 9
$$h = \frac{m \times C_p}{A \times \tau}$$

620
 621 Using:
 622 m = 0.049 kg (The mass of an MJ1)
 623 τ ~ 638 s (As obtained from fits)
 624 C_p = 960 J / kg / K (From Maleki et al. <https://doi.org/10.1149/1.1391704>)
 625 A = 0.004 m² (Assuming perfect cylinder with flat caps)
 626

627 Into (4), yields an effective heat transfer coefficient:
 628

629 h = 17.6 W / m² / K (Calculated from this work)
 630

631 Which is comparable to the reference above:
 632

633 h = 13.4 W / m² / K (Reported by Maleki et al.²¹).
 634

635 **Methods references**

- 636 24. Heenan, T. M.M., et al. Data for an Advanced Microstructural and Electrochemical Datasheet
637 on 18650 Li-ion Batteries with Nickel-Rich NMC811 Cathodes and Graphite-Silicon Anodes.
638 Data in Brief. Volume 32, 106033, (2020).
639 <https://doi.org/10.1016/j.dib.2020.106033>
640
- 641 25. Vaughan, G.B.M., et al. ID15A at the ESRF - a beamline for high speed operando X-ray
642 diffraction, diffraction tomography and total scattering. J. Appl. Cryst. 27, 515-528 (2020).
643 <https://doi.org/10.1107/S1600577519016813>
644
- 645 26. Ashiotis, G., et al. The Fast Azimuthal Integration Python Library: PyFAI. J. Appl. Cryst. 48,
646 2, 510-519, (2015).
647 <https://doi.org/10.1107/S1600576715004306>
648
- 649 27. Coelho, A. TOPAS and TOPAS-Academic: an optimization program integrating computer
650 algebra and crystallographic objects written in C++. J. Appl. Cryst. 51, 210-218 (2018).
651 <https://doi.org/10.1107/S1600576718000183>
652
- 653 28. Finegan, D., et al. Spatial dynamics of lithiation and lithium plating during high-rate
654 operation of graphite electrodes. Energy Environ. Sci., 13, 2570-2584 (2020).
655 <https://doi.org/10.1039/d0ee01191f>
656
- 657 29. Morad, G., et al. High efficiency multichannel collimator for structural studies of liquids and
658 low-Z materials at high pressures and temperatures. Rev. Sci. Instrum. 82, 023904 (2011)
659 <https://doi.org/10.1063/1.3551988>
660
- 661 30. Yaoita et al. Angle-dispersive diffraction measurement system for high-pressure
662 experiments using a multichannel collimator. Rev. Sci. Instrum. 68 (5), (1997)
663 <https://doi.org/10.1063/1.1505104>
664
665

666 **Extended Data Figure legends**

667

668 **Extended Data Fig. 1: Experimental set-up and electrochemical cycling data collected using the operando**

669 **cell holder.**

670

671 a, A photograph of the cell holder with electrical connections as mounted on the diffractometer at the ESRF ID15A
672 and an example of the X-ray diffraction rings collected from the cells. b, Example diagram of the sample-detector
673 geometry used for all experiments: the x-ray beam is directed along x and normal to the detector plane; sample
674 translation perpendicular to the beam goes along y; ω is the angle about the rotation axis. c, A schematic image
675 of the cell holder with electrical terminals (red/black) and 18650 cell. d, Electrochemical data obtained using the
676 cell holder during characterisation at various C-rates.

677

678 **Extended Data Fig 2: X-ray diffraction data collected on MJ1 cell using the operando cell**

679 **holder for SoC calculations.**

680

681 Diffraction patterns for the 8 zones in which the battery volume was divided at initial discharged state,
682 final charged state. For each current applied during discharge (3.5A, 5.25A, 7.0A, 10.0A) the patterns
683 are shown at $\text{Li } x = 0.5$. It is possible to distinguish the four graphite stages and their distribution
684 depending on the discharge current applied.

685

686 **Extended Data Fig 3. Strain components.**

687

688 a, Ewald's sphere construction and its relation to the scattering vector. b, Strain ellipsoid. c, Intersection
689 of the Ewald's sphere and the strain ellipsoid before (black) and after (blue) rotation of the sample
690 around the z axis.

691

692 **Extended Data Fig. 4: Resolving mechanical strain using XRD-CT.**

693

694 **a**, Semi-transparent volume render of the 18650 cell indicating the spatial location of the cross-section.
695 **b,c**, A sub-sectioned volume render of the cell indicating (b) the location and (c) the magnitude of the
696 inflection point feature. **d,e,f,g**, A horizontal greyscale ortho-slice cross-section taken near the cell base
697 as indicated in (a), with reference to three magnified regions (e) before, (f) during and (g) after the
698 inflection. **h**, Another greyscale ortho-slice taken but in the orthogonal (vertical) plane. The vertical
699 strain component calculated on the two 18650 cells (NMC and LFP) from the Cu d-spacing difference
700 before and at the end of repeated charges at 1C rate after 1h relaxation. Multiple 1C charges were
701 compared to understand the influence of successive cycles. The cell volume was again divided in 8
702 circular zones to understand the strain variation distribution inside the battery. **i,j**, show strain on Cu
703 current collector d-spacing at the end of 1C charges as a function of 8 circular zones inside the **i**, NMC
704 and **j**, LFP cells. Notice the strain caused by volume change during graphite-silicon composite anode
705 lithiation is some orders higher than LFP cell graphite lithiation.

706

707 **Extended Data Fig. 5: Resolving SoC using XRD-CT.**

708

709 **a,b,c**, Cross-sections of the cell as schematics of the (a) the outer and (b) the inner zones, and (c) an
710 XRD-CT heatmap of the local SoC at 2.5 V, where blue = low SoC and red = high SoC, for qualitative
711 purposes. **d-k**, The extent of lithiation by quantifying the x in Li_xC_6 for the inner (light gold) and outer
712 (dark gold) regions at the (d,g,h,j) top and (e,g,i,k) bottom of charge for C-rates of (d,e) 0.5C, (f,g) 1.0C,
713 (h,i) 1.5C and (j,k) 2.0C.

714

715 **Extended Data Fig. 6: Degree of lithiation within the MJ1 18650 anode at the bottom of 1C**

716 **discharge.**

717

718 Note: only a section of data is reported here displaying the lithiation states within the eight zones
719 immediately after the 1C discharge.

720

721 **Extended Data Fig.7: SoC quantifications within the MJ1 18650 at high rates.**

722

723 The electrical current (top), anode lithiation (middle) and cathode unit cell expansion (bottom) for the
724 first charge (a) and four subsequent discharges (d-e) at increasing C-rates.

725

726 **Extended Data Fig.8: Comparing internal temperatures within the two 18650 cells.**

727 A repeat of the data presented in Fig. 2b obtained from the NMC cell, with comparison to the LFP cell.

728 Radial zones are shown. All temperature values are reported as the temperature difference between a
729 point in the cell and the ambient temperature.

730

731 **Extended Data Fig. 9: The multi-channel collimator.**

732

733 **Top**, schematic and working principle of the multi-channel collimator (MCC) used for *operando*
734 experiments adapted from [28,29]. The expression for the length of the gauge volume, δx , is given for
735 a pencil beam as a function of front slit opening (a) inner, outer slit radii (r_1 , r_2) and scattering angle
736 (2θ).

737

738 **Bottom**, detail of the gauge volume indicated in the top panel, along with the expressions for gauge
739 volume dimensions in the case of a primary beam of width δy ; a, r_1 , r_2 , and 2θ have the same meaning
740 as in the panel above.

741

742 **Extended Data Fig. 10: Examining the influence of the MCC acquisition.**

743

744 Comparison of MJ1 diffraction patterns obtained without the MCC (black), and with the MCC (red).
745 Inset: full range of the MJ1 diffraction patterns with and without MCC, along with the calculated
746 intensity from the gauge volume selected with the MCC.

747

748

749 **Data and code availability**

750

751 Correspondence and requests for materials should be addressed to the corresponding author: Professor
752 Paul R Shearing.

753

754 **Acknowledgements**

755

756 This work was carried out with funding from the Faraday Institution (faraday.ac.uk; EP/S003053/1),
757 grant number FIRG001 and FIRG003. The authors would like to acknowledge the Royal Academy of
758 Engineering (CiET1718\59) for financial support. Use of the instruments was supported by
759 EP/N032888/1. The ESRF is acknowledged for provision of beamtime (ME-1577: 10.15151/ESRF-ES-
760 549494442, IH-MA-171: 10.15151/ESRF-ES-532206404, IH-MA-153: 10.15151/ESRF-ES-
761 478854138). M.J acknowledges HORIBA-MIRA, UCL and EPSRC (EP/R513143/1) for a CASE
762 studentship. This project has received funding from the European Union’s Horizon 2020 research and
763 innovation programme under the Marie Skłodowska-Curie grant agreement “InnovaXN” No 847439.
764 The authors would like to thank Mohamed Mezouar (ESRF) for lending of the MCC and related
765 equipment, and Denis Duran, Emmanuel Papillon and Dr. Partha Paul for beamline support.
766

767 **Author contributions**

768

769 TH led the investigation. TH, MDM, PS conceived the experiments. TH, IM, AL, CT, SC, MDM, M.J.,
770 A.J, GG performed the experiments, TH, IM, AL, CT, SC, MDM, M.J., A.J. performed the data
771 analysis. MDM leads work at ESRF as the Scientist in Charge of ID15A. RJ leads work as the
772 Degradation Project Manager for the Faraday Institution. PS and DB lead all work from the
773 Electrochemical Innovation Lab (UCL) and sourced all funding to support this work.
774

775 **Competing interest declaration**

776

777 There are no competing interests known to the authors to declare.

778

779 **Additional information**

780

781 Supplementary information is available for this paper.

782

783 **Corresponding author**

784

785 Professor Paul R Shearing, p.shearing@ucl.ac.uk

786